The Influence of Sheet Metal Anisotropy on Laser Forming Process

Peng Cheng

Y. Lawrence Yao

Department of Mechanical Engineering,
Columbia University,
220 Mudd Building, MC 4703,
New York, NY 10027

Cold-rolled sheet metal that is often used in laser forming exhibits anisotropic properties, which are mostly caused by preferred orientations of grains developed during the severe plastic deformation such as cold rolling. In the present study, the textures of cold-rolled mild steel sheets are characterized and the influence of the plastic anisotropy on laser forming process is investigated. Deformation textures are measured in terms of pole figures and orientation distribution function (ODF) plots obtained through electron backscatter diffraction (EBSD). The anisotropy index (R-value) of the material with different rolling reductions is obtained by uniaxial tensile tests. Both are compared and agree with the texture development theory. Effects of the plastic anisotropy on bending deformation during the laser forming process are investigated experimentally and numerically. Various conditions including different laser power, scanning speed, and number of scans for sheets of different rolling reductions are considered and results are discussed. The simulation results are consistent with the experimental observations.
[DOI: 10.1115/1.1949620]

1 Introduction

Laser forming is a flexible rapid prototyping and low-volume manufacturing process, which uses laser-induced thermal distortion to shape sheet metal parts without tooling or external forces. Laser forming provides the potential for many technological advantages as compared to the conventional forming technologies [1], including design flexibility, production of complex shapes, forming of thick plates, and possibility of rapid prototyping. Numerical and experimental investigations of laser forming processes were carried out to better understand process mechanisms and the effects of key process parameters on dimension and mechanical properties of the formed parts. Vollertsen [2] identified three key mechanisms [temperature gradient mechanism (TGM), buckling mechanism (BM), and upsetting mechanism (UM)] to explain the thermomechanical behavior in laser forming, each associated with specific combinations of component geometries and laser process conditions. Studies of material property effects on the laser forming process were reported, such as influence of strain hardening [3], strain rate effects [4], and microstructure evolution in laser forming [5]. The effects of anisotropy on the laser forming process, however, have not been studied in detail, while most sheet metal materials used in the laser forming are cold-rolled.

Anisotropy includes elastic and plastic anisotropy. In cold-rolled sheets, elastic deformation is much smaller compared with the plastic deformation, so only the anisotropic plasticity is normally considered. The type of plastic anisotropy usually desired in sheet metal forming is that the sheet is isotropic in the plane and has an increased strength in the thickness direction, which is normally referred to as normal anisotropy. More often, however, the type of plastic anisotropy is characterized by different strengths in different directions in the plane of the sheet as well, which is called planar anisotropy. This is simply because of the different amount of deformation along the rolling and other directions in the plane. The plastic anisotropy is commonly characterized by R-values, which will be explained in more detail in later sections. In this study, the planar plastic anisotropy is dealt with and simply referred to as anisotropy.

The primary source of plastic anisotropy comes from the texture or the preferred crystallographic orientations of the grains as a result of cold rolling. The plastic anisotropic properties of sheet metals have generally been investigated independently by two approaches [6]. The first one is to develop various macroscopic yield functions from a phenomenological viewpoint. The second approach is to develop polycrystal models based on the constitutive behavior of crystalline slip in single crystals.

Many phenomenological yield criteria have been proposed in the past to account for plastic anisotropy, among which Hill's quadratic yield criterion [7] has been widely used. Gotoh [8] proposed a fourth-order polynomial criterion used for plane stress analysis. Barlat and Lian [9] proposed a tricomponent yield criterion. Hill [10] developed an improved plane-stress yield criterion for orthotropic sheet metals. The latter three yield functions were proposed only for plane stress analysis. Further detail on plastic anisotropy yield criterion can be found in Ref. [11]. From a microscopic viewpoint, various polycrystal models based on crystalline slip have been developed, among which a Taylor-type model [12] is widely used, in which the fundamental assumptions is the strain field in each grain being homogeneous and the same as that of the aggregate. A relaxed constraint (RC) model was proposed by Kocks and Chandra [13] in which fewer active slip systems were assumed compared with the Taylor model. To overcome the ambiguity in the selection of active slip systems, a rate sensitive model has been used for the deformation texture modeling [14]. Although the studies on anisotropy have been investigated both macroscopically and microscopically, the effect of anisotropy on laser forming has not been investigated specifically.

In the present study, the effect of anisotropy exhibited in cold-rolled mild steel sheets on laser forming process is investigated. To better characterize the anisotropy, pole figures and orientation distribution function (ODF) plots of steel sheet were obtained by electron backscatter diffraction (EBSD) and compared with those predicted by deformation texture theories. R-values were measured and compared with those predicted by theories. Effect of such anisotropy on laser forming under various conditions, such

Contributed by the Manufacturing Engineering Division for publication in the ASME Journal of Manufacturing Science and Engineering. Manuscript received September 10, 2003; final revision received July 28, 2004. Associate Editor: K. Rajurkar.

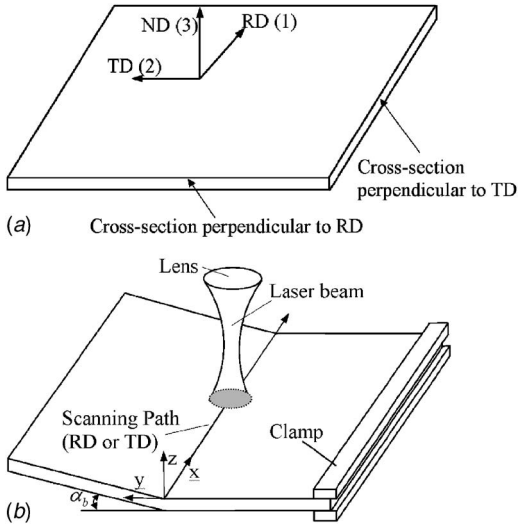

Fig. 1 (*a*) Rolled-sheet coordinate system and terminology: RD, rolling direction; TD, transverse direction; and ND, normal direction; and (*b*) schematic laser forming system scanning path along the RD or TD

as different sheet thickness reductions, scanning speed, laser power, as well as multiple scanning were experimentally and numerically investigated.

2 Background

2.1 Deformation Textures in bcc Cold-Rolled Sheet Metals. Sheet texture is described by the Miller index notation $(hkl)[uvw]$, in which the crystallographic plane (hkl) is roughly parallel to the sheet surface, and the direction $[uvw]$ in that plane is roughly parallel to the rolling direction (RD) [Fig. 1(*a*)]. Various types of textures are possible to form in cold-rolled sheet metal depending on material type and processing condition. Both experimental and simulation results have shown that four texture components, $\{001\}\langle 110\rangle$, $\{112\}\langle 110\rangle$, $\{111\}\langle 112\rangle$, and $\{111\}\langle 110\rangle$, are possible in cold-rolled body centered cubic (bcc) metals of initially random textures [15]. Which texture components in bcc metals are present and more dominant also depends on process condition [16,17]. For instance, when rolling reduction is moderate (i.e., $<70\%$), $\{001\}\langle 110\rangle$ and $\{112\}\langle 110\rangle$ are the dominant components on the α-fiber, that is, $\langle 110\rangle$ is parallel along the RD, and one sees a weak preference of $\{111\}\langle 112\rangle$ on the γ-fiber, that is, $\{111\}$ is parallel along the normal direction (ND) of the sheet. For large rolling reduction (i.e., $>70\%$) the maximum on the α-fiber is shifted to $\{112\}\langle 110\rangle$ and that on the γ-fiber from $\{111\}\langle 112\rangle$ to $\{111\}\langle 110\rangle$.

To quantitatively predict the development of textures, several models were developed. The most widely applied model is a Taylor-type model, which assumes that the strain of the individual crystallite is equal to the strain of the polycrystalline aggregate and is therefore called the "Full Constraint" (FC) model. In Taylor's model, the work increment done during the tension process in terms of the macroscopic stress σ_p and the strain increments $d\varepsilon$ equals to the internal work done by the critical shear stress $\tau_0^{(r)}$ and shear strain increments $d\gamma^{(r)}$ in the rth slip system ($r=1,2,\ldots,5$).

$$\sigma_p d\varepsilon = \sum_{r=1}^{5} \tau_0^{(r)} d\gamma^{(r)} \tag{1}$$

Assuming the critical shear stress $\tau_0^{(r)}$ is the same for all slip systems and equal to τ_0. The Taylor factor can be defined as

$$M = \frac{\sigma_p}{\tau_0} = \frac{\sum_{r=1}^{5} d\gamma^{(r)}}{d\varepsilon} \tag{2}$$

Taylor factor M can be compared with the reciprocal of the Schmid factor. Combinations of slip systems with the minimum Taylor's factor will be the active slip systems in the plastic deformation.

Deformation textures calculated according to the Taylor model are in fairly good qualitative agreement with the observed ones. However, some discrepancies exist when it was applied in large reduction cases. "Relaxed Constraint" (RC) models were developed to describe texture development in large deformation. Unlike the Taylor approach where strain compatibility is strictly prescribed, in the RC models partial constraints are imposed on the basis of mixed boundary conditions: some components of strain and the others of stress are presumed given. For cold rolling with large reduction, the RC models are more accurate to predict the texture development compared with the FC model.

2.2 Anisotropic Mechanical Behavior. Sheet metals with textures exhibit anisotropic mechanical behavior, of which the two most important measures are R-value and anisotropic yielding stress. They are related by the anisotropy yield criterion (Sec. 3.4). R-value is defined to express different contractile strain ratio and is generally applied as an index of anisotropy.

$$R = d\varepsilon_w / d\varepsilon_t \tag{3}$$

where subscripts w and t refer to the width and thickness directions in a sheet tensile specimen extended in the length or l direction. Although R-value is commonly used to describe material anisotropy, analysis of possible behavior is often more convenient with a parameter ρ, defined as:

$$\rho = -d\varepsilon_w / d\varepsilon_l \tag{4}$$

To characterize the relations between the anisotropy and the textures, Taylor factor M, which represents the relative strengths of different orientations and textures, can be rewritten as

$$M = (1/\tau) dw / d\varepsilon_l \tag{5}$$

where $dw/d\varepsilon_l$ is the plastic work per volume for a differential strain $d\varepsilon_l$, and τ is the shear stress required for slip within the crystals. By this definition, M can be expressed as a function of ρ. Since M is also known as a function or crystal orientation, relations between textures and anisotropy parameters can be obtained by M-ρ curves. Since the material will elongate with the least expenditure of energy, the lowest value of M should be the appropriate one for uniaxial tension, and the corresponding value of ρ should describe the expected shape change. Then by the assumption of constant volume ($d\varepsilon_l + d\varepsilon_w + d\varepsilon_t = 0$), R value can be determined by

$$R = \rho/(1-\rho) \tag{6}$$

The above predictions are for ideal textures. The quantitative analysis of texture by the orientation distribution function (ODF) makes it possible to directly predict the relationship between texture and anisotropic properties. A general expression for the orientation dependent macroscopic property $\bar{E}(g')$ in the orientation g' is

$$\bar{E}(g') = \int E(g) f(g) dg \tag{7}$$

where Euler space $g=\{\varphi_1, \phi, \varphi_2\}$, $E(g)$ is the orientation dependent property of a crystallite, and $f(g)$ describing the distribution of crystalline lattice orientations. This equation has been successfully used to predict plastic, elastic, and magnetic anisotropy.

3 Experimental and Simulation

3.1 Texture Measurement. Texture measurements of AISI 1010 cold-rolled steel sheets 1.4 mm and 0.89 mm thick were carried out using electron backscatter diffraction (EBSD). A series of typical scans were recorded with a step size of 3 μm and consisted of 3000–6000 indexed points. Four incomplete pole figures {100}, {110}, {111}, and {112} were measured in the rolling plane (RD-TD plane where TD stands for transverse direction). Three-dimensional orientation distribution functions (ODFs) $f(g)$ were calculated by using the spherical harmonics. The ODFs are represented in three-dimensional Euler space in the range of 0 deg $\leqslant \varphi_1, \phi, \varphi_2 \leqslant 90$ deg by way of isointensity contour lines in different sections with an Euler angle held constant. Grain structures in different cross sections were observed by scanning electron microscope (SEM). Samples were polished and etched using 3% HNO_3 for 5 s for EBSD and 20 s for SEM.

3.2 Measurement of *R*-Values. In accordance with the ASTM Standard E517, the *R*-values of AISI 1010 cold-rolled steel sheets 1.4 mm and 0.89 mm thick were measured by uniaxial tensile test on a material testing machine. The specimens were cut by a CNC machine with axes along the rolling direction (RD), transverse direction (TD), and 45 deg to the rolling direction, corresponding to the measurement of R_0, R_{45}, and R_{90}, where the subscripts represent the angle to the rolling direction. The specimens have gage length of 1.6 in. (40.64 mm) and width of 0.4 in. (10.16 mm). Due to the difficulty in measuring gage thickness changes with sufficient precision [Eq. (3)], an equivalent relationship is commonly used, based on length and width strain measurements:

$$R = \frac{\varepsilon_w}{-(\varepsilon_l + \varepsilon_w)} = \frac{\ln(w_i/w_f)}{\ln(l_f w_f / l_i w_i)} \tag{8}$$

where ε_w and ε_l are true strains in width and length directions, w_i, w_f and l_i, l_f are initial and final gage width and length, respectively. With most materials the change of R with strain ε_l is negligible [11].

The R value is a very sensitive measure. Small errors in the measured strains cause a large error in the determined R value. Measurement accuracy is improved as the strain is increased but within the necking limits [18]. According to Eq. (8) the variation of the R-value can be expressed as

$$v(R) = \frac{s(R)}{R} = (1+R)\left[\frac{s(\varepsilon_w)^2}{\varepsilon_w^2} + \frac{s(\varepsilon_l)^2}{\varepsilon_l^2}\right]^{1/2} \tag{9}$$

where $s(R)$, $s(\varepsilon_w)$, and $s(\varepsilon_l)$ stand for the standard deviation of R, ε_w, and ε_l, respectively. And the standard deviation of ε_w can be written as

$$s(\varepsilon_w) = \sqrt{\frac{s(w)^2}{w_0^2}[\exp(-2\varepsilon_w)+1]} \quad \text{if } s(w_f) = s(w_0) = s(w) \tag{10}$$

$s(\varepsilon_l)$ can be obtained similarly. Then the variation of R-values can be further expressed as

$$v(R) = \frac{1+R}{\varepsilon_l}\left\{ v(w_l)^2\left(\frac{1+R}{R}\right)^2[1+\exp(-2\varepsilon_w)] + v(l_i)^2[1+\exp(-2\varepsilon_l)^2]\right\}^{1/2} \tag{11}$$

from which it is seen that since the variations of measurement of initial and final dimensions are unavoidable, a higher plastic strain will reduce the effect of dimension measurement errors on that of R-value. Commonly 10%–20% plastic strains are utilized in determining the R-value of low carbon steels. In the present study, approximate 15% plastic strain is utilized. The strain rate in the uniaxial tensile tests was taken to be 1.25×10^{-3}/s, which is within the range of the ASTM Standard ($<8.33\times10^{-3}$/s).

3.3 Laser Forming Experiments. The material is cold-rolled AISI 1010 steel, and the workpiece size is 80 mm $\times$ 80 mm with thickness of 1.4 mm and 0.89 mm. Experiments of straight-line laser forming were carried out along the RD and TD, respectively [Fig. 1(*b*)]. The laser system used in the experiments is a PRC-1500 CO_2 laser, with a maximum output power of 1.5 kW and power density distribution is Gaussian (TEM_{00}). In the present study, various conditions such as different material reduction (corresponding to two different workpiece thickness levels), different scanning speed (from 50 mm/s to 90 mm/s), different laser power (from 600 W to 800 W) and number of scans (1 and 10) were applied. Laser beam diameter varied from 6 mm to 4 mm when the sample thickness changed from 1.4 mm to 0.89 mm. A coordinate measuring machine (CMM) is used to measure the bending angle at different positions along the scanning path. To enhance laser absorption by the workpiece, graphite coating is applied to the surface exposed to the laser.

3.4 Numerical Simulation. In numerical simulation the laser forming process is modeled as a sequentially coupled thermal-mechanical process. In the thermal analysis, the transient conduction for a solid workpiece irradiated by a laser beam can be expressed in terms of temperature as

$$\rho c_p \frac{\partial T}{\partial t} = \nabla \cdot (k \nabla T) \tag{12}$$

where ρ, c_p, and k are the density, specific heat, and thermal conductivity, respectively. The heat flux due to the Gaussian laser power is expressed as

$$F = Q_{\max} \exp(-R_k R^2) \text{ and } Q_{\max} = P_{\text{laser}} R_k / \pi \tag{13}$$

where $Q_{\max}$ is the heat flux intensity of the laser beam, R is the distance to the laser beam center, R_k is the concentration coefficient, and P_{laser} is the laser power.

All the surfaces of workpiece subject to the convective heat flux that is $f=h(T-T_s)$, where h is the convective heat transfer coefficient, T is the surface temperature, and T_s is the surrounding temperature. The radiation heat flux is also considered at the heating surface which is $f_c=\varepsilon\sigma(T^4-T_s^4)$, where ε and σ are emissivity and Stefan-Boltzmann constant, respectively.

In the mechanical analysis, the deformation of a material during laser forming depends on the magnitude of stress, strain, and strain rate. Due to the elevated temperature in the laser forming process, the strain rate has a much higher effect on the material flow stress than at lower temperature, which in turn, influences the deformation of the material.

The total strain rate during laser forming can be decomposed into $\dot{\varepsilon}_{ij}=\dot{\varepsilon}^e_{ij}+\dot{\varepsilon}^p_{ij}+\dot{\varepsilon}^{\text{th}}_{ij}+\dot{\varepsilon}^c_{ij}$, where $\dot{\varepsilon}_{ij}$, $\dot{\varepsilon}^e_{ij}$, $\dot{\varepsilon}^p_{ij}$, $\dot{\varepsilon}^{\text{th}}_{ij}$, and $\dot{\varepsilon}^c_{ij}$ represents total strain rate, elastic strain rate, plastic strain rate, thermal strain rate, and creep strain rate. Due to the short thermal cycles in laser forming, the creep can be neglected. Therefore, the term $\dot{\varepsilon}^c_{ij}$ vanishes. The thermal strain rate can be expressed as $\dot{\varepsilon}^{\text{th}}_{ij}=\alpha\dot{T}\delta_{ij}$, where α is the thermal expansion coefficient and $\dot{T}$ is the rate of change of temperature. By combining the elastic strain rate, plastic strain rate, and thermal strain rate components, the total strain rate can be expressed as

$$\dot{\varepsilon}_{ij} = \frac{1+\nu}{E}\dot{\sigma}_{ij} - \delta_{ij}\frac{\nu}{E}\dot{\sigma}_{kk} + \lambda\left(\sigma_{ij} - \delta_{ij}\frac{\sigma_{kk}}{3}\right) + \delta_{ij}\alpha\dot{T} \tag{14}$$

where ν is Poisson ratio, E, the Young's modulus, λ the proportional factor, and α the thermal expansion.

For anisotropic analysis Hill's potential function is applied instead of Von Mises function. Hill's function is expressed in terms of rectangular Cartesian stress components as

$$f(\sigma) = \sqrt{F(\sigma_{22} - \sigma_{33})^2 + G(\sigma_{33} - \sigma_{11})^2 + H(\sigma_{11} - \sigma_{22})^2 + 2L\sigma_{23}^2 + 2M\sigma_{31}^2 + 2N\sigma_{12}^2} \quad (15)$$

where 1, 2, and 3 represent the rolling, transverse, and normal directions, respectively. F, G, H, L, M, and N are constants obtained by material tests in different orientations. They are defined as

$$F = \frac{1}{2}\left(\frac{1}{P_{22}^2} + \frac{1}{P_{33}^2} - \frac{1}{P_{11}^2}\right), \quad G = \frac{1}{2}\left(\frac{1}{P_{33}^2} + \frac{1}{P_{11}^2} - \frac{1}{P_{22}^2}\right),$$

$$H = \frac{1}{2}\left(\frac{1}{P_{11}^2} + \frac{1}{P_{22}^2} - \frac{1}{P_{33}^2}\right) \quad (16)$$

$$L = \frac{3}{2P_{23}^2}, \quad M = \frac{3}{2P_{13}^2}, \quad N = \frac{3}{2P_{12}^2}$$

where P_{ij} are ratios of measured yield stress to the reference yield stress. In sheet metal forming applications plane stress condition is generally assumed. Relative to coordinates along the principal directions of orthotropy, the Hill's yield criterion can be written as

$$(G+H)\sigma_{11}^2 - 2H\sigma_{11}\sigma_{22} + (H+F)\sigma_{22}^2 + 2N\sigma_{12}^2 = 1 \quad (17)$$

The flow rule for this potential defines the incremental strain as

$$d\varepsilon_{11} = d\lambda[(G+H)\sigma_{11} - H\sigma_{22}],$$

$$d\varepsilon_{22} = d\lambda[(F+H)\sigma_{22} - H\sigma_{11}], \quad (18)$$

$$d\varepsilon_{33} = d\lambda[-G\sigma_{11}]$$

In a simple tension test performed in the rolling direction in the plane of the sheet, the incremental strain ratio can be written as

$$d\varepsilon_{11}:d\varepsilon_{22}:d\varepsilon_{33} = (G+H):(-H):(-G) \quad (19)$$

According to the definition of R-value [Eq. (3)], it is obtained

$$\frac{H}{G} = \frac{d\varepsilon_{22}}{d\varepsilon_{33}} = R_0. \quad (20)$$

Similarly, for a simple tension test performed in the 90 deg and 45 deg to the rolling direction,

$$\frac{H}{F} = R_{90} \text{ and } \frac{N}{G} = \left(\frac{1}{2} + R_{45}\right)\left(1 + \frac{R_0}{R_{45}}\right) \quad (21)$$

Then the yield stress ratio used in Hill's potential function can be expressed in terms of R-values, assuming the yield stress ratio in the rolling direction is 1,

$$P_{11} = 1, \quad P_{22} = \sqrt{\frac{R_{90}(R_0+1)}{R_0(R_{90}+1)}}, \quad P_{33} = \sqrt{\frac{R_{90}(R_0+1)}{(R_0+R_{90})}}$$

$$\text{and} \quad P_{12} = \sqrt{\frac{3(R_0+1)R_{90}}{(2R_{45}+1)(R_0+R_{90})}} \quad (22)$$

In numerical simulation, the main assumptions used are as follows. Plastic deformation generated heat is small as compared to energy input in laser forming so that it is negligible. During the entire laser forming process, no melting takes place. The symmetric plane is assumed to be adiabatic. ABAQUS was used to complement the numerical simulation and sequentially coupled thermal and mechanical models were applied. The same mesh model was used for the thermal and mechanical deformations. A 20-nodes brick element was used in the mechanical analysis because this kind of element has no shear locking and hourglass stiffness and is also suitable for bending-deformation-dominated processes such as laser forming. In order to remain compatible with the structural analysis, an element, DC3D20, is used in heat transfer analysis. A user subroutine of dflux was developed in numerical simulation. This subroutine was used to define a Gaussian distribution laser-induced flux as a function of position and was called at each flux integration point during heat transfer procedure.

4 Results and Discussion

4.1 Texture Characterization. Figure 2(*a*) shows the four incomplete pole figures {100}, {110}, {111}, and {112} of the cold-rolled steel sheet with thickness of 1.4 mm. In the normal direction (ND), a stronger component of {111} and weaker components of {001} and {112} were seen. In the rolling direction (RD), a stronger ⟨110⟩ direction and weaker ⟨001⟩ and ⟨112⟩ directions were identified. Three major components of textures {111}⟨110⟩, {112}⟨110⟩, and {001}⟨110⟩ were therefore determined, while in the subsequent orientation distribution function (ODF) plots with more exact components were obtained.

Figure 2(*b*) shows ODF sections (with φ_2 increments from 0 deg to 85 deg) for the same material by EBSD. Most of deformation textures can be found with higher intensity around φ_2=45 deg section, as shown in Fig. 3. The α-fiber textures are $(112)[1\bar{1}0]$ and $(001)[1\bar{1}0]$ and the γ-fiber textures are $(111)[0\bar{1}1]$ and $(111)[\bar{1}\bar{1}2]$. This observation is consistent with the texture development theory (Sec. 2.1).

Figure 4 shows the {100}, {110}, {111}, and {112} pole figures obtained from steel sheet 0.89 mm thick which represents larger rolling reduction. The obvious difference can be found in {100} pole figure compared with that of 1.4 mm steel sheet. {001} texture has disappeared and ⟨110⟩ is the major direction along the rolling direction. From ODF plots, the major components of textures are determined as the α-fiber $(112)[1\bar{1}0]$ to $(111)[1\bar{1}0]$ and γ-fiber $(111)[0\bar{1}1]$. The change of texture components is consistent to the texture development theory. That is, when rolling reduction is higher, the maximum on the α-fiber is shifted to {112}⟨110⟩ so that {001}⟨110⟩ components can be neglected. In the γ-fiber the components of textures shift from {111}⟨112⟩ to {111}⟨110⟩.

The grain structure at different cross sections of the cold-rolled sheet was observed by scanning electron microscope (SEM). Figure 5 shows the grain structures in cross sections perpendicular to the TD and RD directions of the cold-rolled steel sheet with thickness of 1.4 mm, respectively. It can be seen that grains are substantially elongated in the rolling direction while no significant changes are seen along the transverse direction. This is due to the deformation characterization of the cold rolling process. In cold rolling plates and sheets with high width-to-thickness ratios, the width of the material remains essentially constant and the length of the material is substantially elongated during rolling.

4.2 Macro Anisotropic Properties, *R*-Value, and Yield Stress. Figure 6(*a*) shows R-values determined in tensile tests for two different sheet reductions and along three different angles to rolling direction. The pattern of R-values between the two reduction levels is somewhat similar but different in the following way. In the lower reduction case (thickness of 1.4 mm), the R-value along the rolling direction (RD), R_0, is larger than that along the transverse direction (TD), R_{90}. While in the higher reduction case (thickness of 0.89 mm), R_0 is slightly smaller than R_{90}. This result is consistent with theoretical predictions.

The prediction of R-values using the series expansion method is generally carried out within the framework of the Taylor's model. To improve the accuracy of predictions, "Relaxed Constraint"

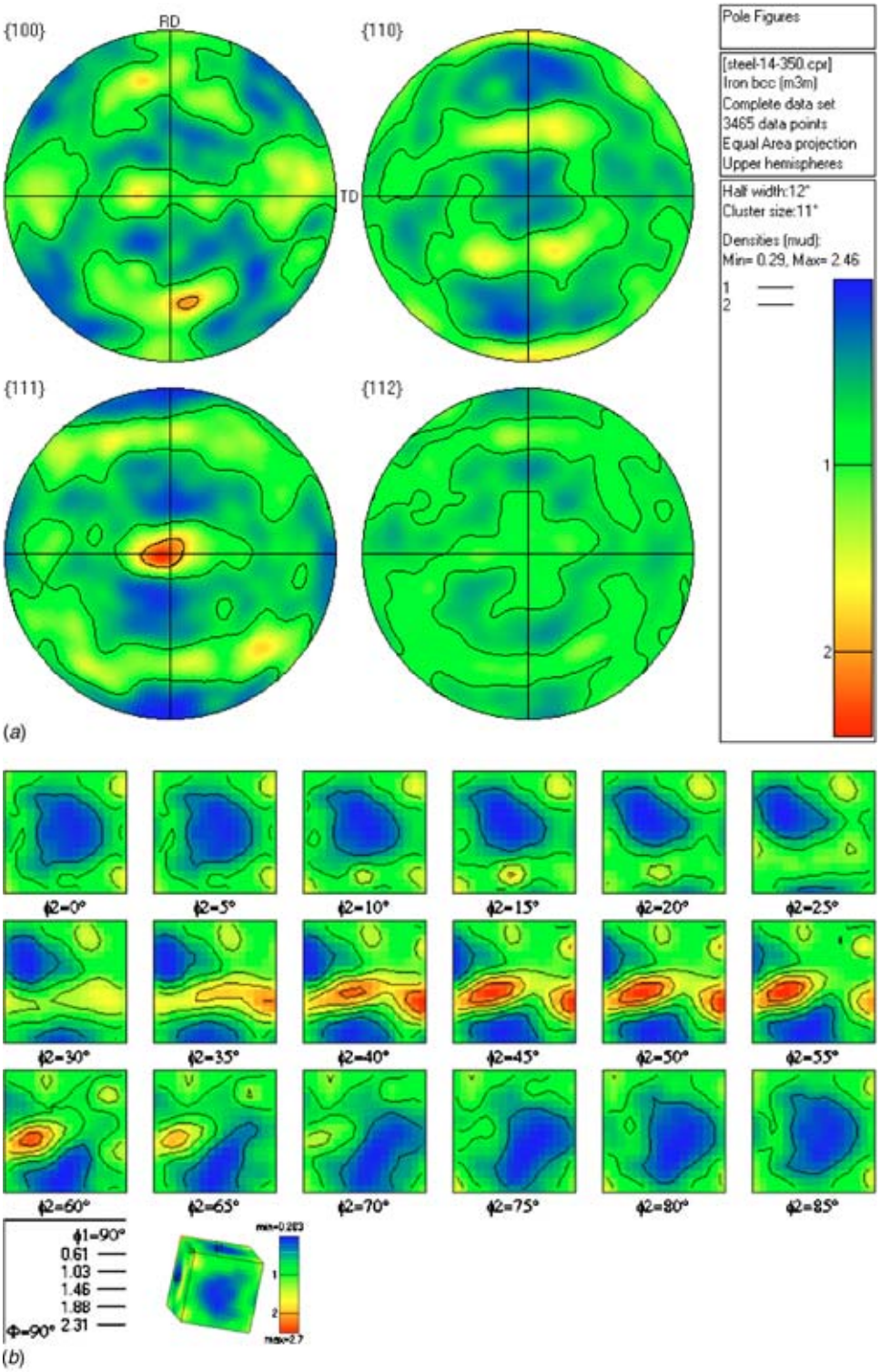

Fig. 2 (*a*) {001}, {110}, {111}, and {112} pole figures of AISI 1010 cold-rolled steel sheet of 1.4 mm thick; and (*b*) orientation distribution functions (ODFs) of the same sample

grain interaction models are employed [19]. The Taylor or full constraint (FC) model has been shown to be more accurate in prediction at lower reduction cases. While in higher reduction cases, the relaxed constraint (RC) model is more accurate due to the more accurate boundary conditions.

From Fig. 6(*a*) a very good agreement can be seen for the lower reduction case (thickness=1.4 mm), while for larger reduction case (thickness=0.89 mm), agreement is again seen for R_0 and R_{90} but some discrepancy between the measured and predicated values is seen for R_{45}. A likely reason for the discrepancy is as follows. It is known that the RC approach is appropriate for describing the deformation of aggregates of pancake-shaped grains. For cold-rolled low carbon steel, the elongated flattened grains are mostly along the rolling direction [Fig. 5(*b*)]. As a result, the predictions obtained from the RC model fit the experimental data somewhat better from 0 deg to 45 deg. For angles above 45 deg,

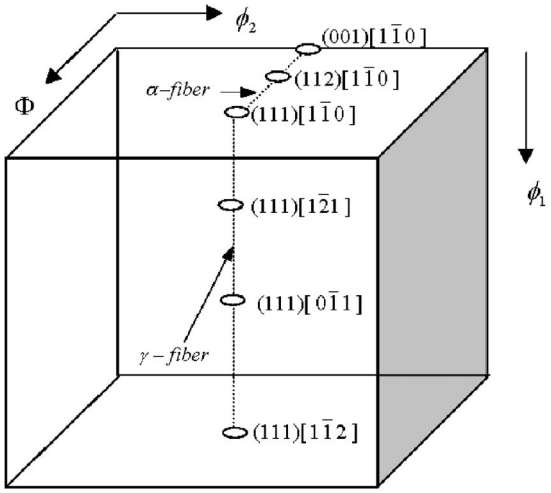

Fig. 3 Euler space (0 deg≤φ_1,Φ,φ_2≤90 deg) for a cubic crystal system and orthorhombic sample system. Two relevant textures fibers are depicted schematically

the grains are no longer elongated along the tensile axis, so that the grain shape argument for using this model is not valid any more.

Figure 6(*b*) compares the yield stresses between indirectly measured values and theoretical predictions. The measured values are obtained by measured *R*-values and Hill's yield criterion [Eq. (22)]. As expected, the prediction based on the FC model fits the lower reduction case closely and that based on the RC model fits the high reduction case closely.

4.3 Anisotropic Effect on Laser Forming Involving Different Material Reductions. 80×80×1.4 mm samples were scanned along either the RD or TD. Figure 7(*a*) shows the experimental and numerical results of bending angles caused by the laser scanning and a reasonable agreement is seen. The experiments were repeated two to three times and the repeatability is shown in terms of error bars around the data points. Bending angles are measured at five equally spaced positions along the scanning direction. The difference between these five points is due to the so-called edge effects which had been thoroughly studied before [20]. But there is obvious difference in bending angle between scanning along the RD and TD. Since the flow stress in TD is smaller than that in RD [Fig. 6(*b*)], the bending angle when scanned along the TD is smaller than that when scanned along RD because it is well known that the plastic deformation perpendicular to the scanning direction is primarily responsible for the bending angle.

To further illustrate the point, Fig. 7(*b*) shows the simulated thermal cycle and the *y*-plastic strain [*y* is perpendicular to the scanning direction as shown in Fig. 1(*b*)] at a location (*x* =21.3 mm) along the scanning path. As expected, the plastic strain is smaller when scanned along the TD than that along the RD. Scanning on the same but hypothetically isotropic material is also superposed for comparison. The isotropic material is assumed to have *R*-values equal to 1 and the yield stress is 30% smaller than that of cold-rolled sheet. The *y*-plastic strain of isotropic material is larger due to the smaller flow stress than that of the anisotropic material.

The bending angle difference of samples with thickness of 0.89 mm is quite different from that of samples with thickness of 1.4 mm. Since in this case the flow stress in the RD is smaller than that of the TD [Fig. 6(*b*)], bending angle is smaller when scanning along the RD than that of scanning along the TD. This is

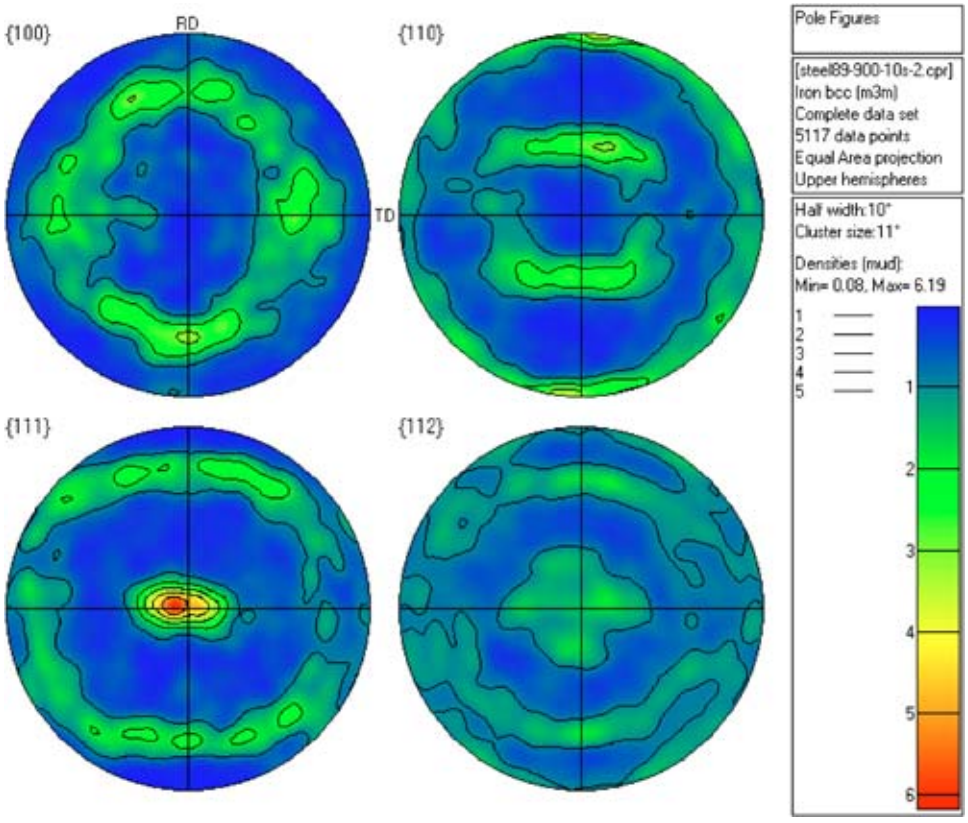

Fig. 4 {001}, {110}, {111}, and {112} pole figures of AISI 1010 cold-rolled steel sheet of 0.89 mm thick

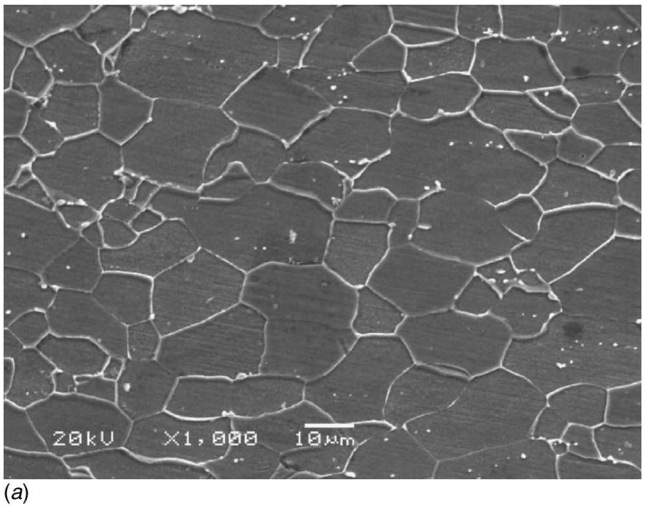

(*a*)

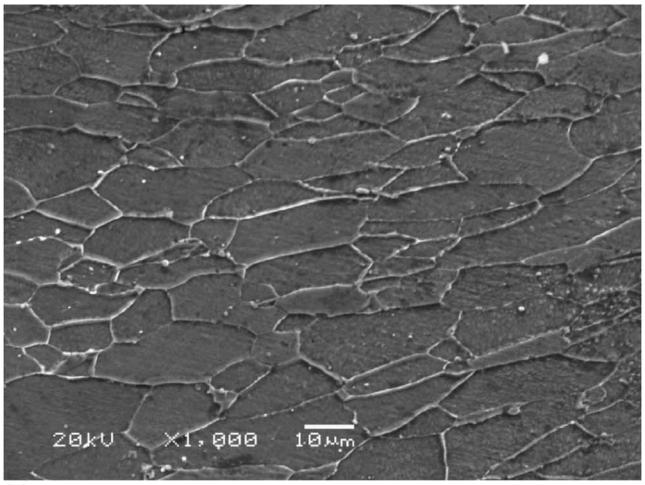

(*b*)

Fig. 5 SEM micrographs of grain structures of cold-rolled AISI 1010 steel 1.4 mm thick (×1000) (*a*) cross section perpendicular to the transverse direction (TD); and (*b*) cross section perpendicular to the rolling direction (RD)

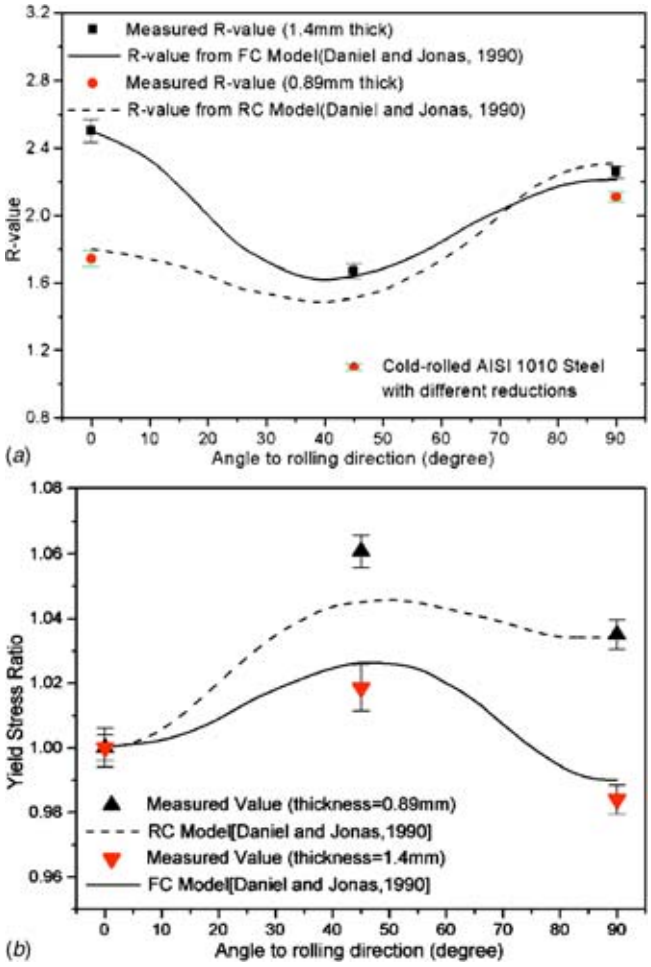

Fig. 6 (*a*) Comparison of *R*-values between theoretical values and measured values; (*b*) comparison of yield stress ratio between theoretical values and calculated values by *R*-values and Hill's criterion

consistent experimentally and numerically as shown in Fig. 8(*a*). Figure 8(*b*) illustrates the time history of plastic strain at a location (x=21.3 mm) along the scanning path and it is seen that bending strain is smaller when scanning along the RD than that of scanning along the TD. The thermal history of that point also shows that the majority of the strains occurred during the cooling cycle. Although the laser power and beam spot size applied on the two types of sample (1.4 mm and 0.89 mm) are different, the thermal cycles on the scanning paths are almost the same due to the same scanning speed and the combination of power and spot size. In summary, the difference of bending deformation exists when scanning along different directions in the anisotropic material used in this study. With the rolling reduction of steel sheet increasing, the anisotropic effect on laser induced bending is more pronounced. Figure 9 compares bending angle difference between scanning along the RD and TD. In 0.89 mm thick samples the bending angle difference is almost 3 times as large as that of 1.4 mm thick samples.

4.4 Anisotropic Effect Under Different Scanning Speeds. Influence of plastic anisotropy on laser forming deformation under various scanning speeds is investigated for the 0.89 mm thick case. Both experimental and numerical results are presented and show agreement. From Fig. 10(*a*), it can be seen that when the scanning speed increases while the laser power is kept constant, the average bending angle decreases whether it was scanned along the RD or TD. This is obviously due to the decreased laser energy input per unit time, which causes decreased temperature rise. At the same time, increased speed increases strain-rate which in turn causes increased flow stress.

However, the bending angle difference between scanning along the RD or TD seems not to change with speed and remains more or less constant within the speed range investigated. Figure 10(*b*) shows the difference and relative difference of bending angles when scanning along the RD or TD under different speeds. The almost constant difference confirms the above observation. The reason for that is, when scanning speed increases, the temperature drop and strain rate increase is almost the same when scanning with the same speed along the RD or TD (Fig. 11). So the flow stress in the RD and TD will increase by a similar amount and the difference of flow stress does not change much in the absolute sense. As a result, the absolute difference of bending angles almost does not change. But if comparing the relative difference of the bending angles, which is defined as the ratio of difference to average bending angles, a clear increasing trend with speed can be seen [Fig. 10(*b*)]. This is because, although the difference of flow stress does not change much with speed, the relative difference increases since the average bending angle decreases with the increasing speed. It is seen that the anisotropic effect increases from 8% to 19% when scanning speed increases from 50 mm/s to 90 mm/s.

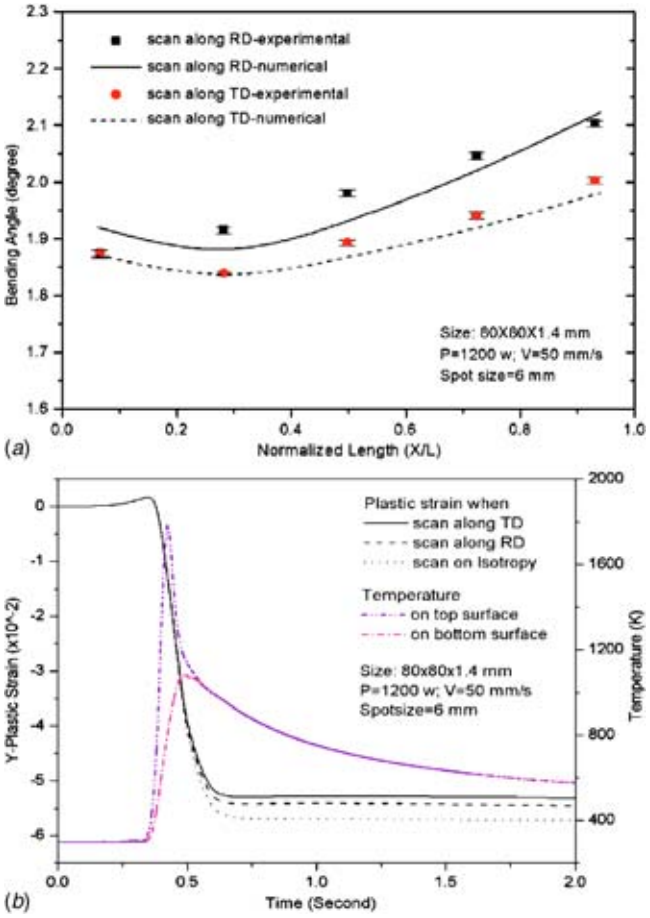

Fig. 7 (*a*) Numerical and experimental bending angles of 1.4 mm thick steel sheet with scanning along the RD and TD, respectively; and (*b*) simulated time history of plastic strain in the *y* direction, which is perpendicular to the scanning path (results on isotropic sheets also included)

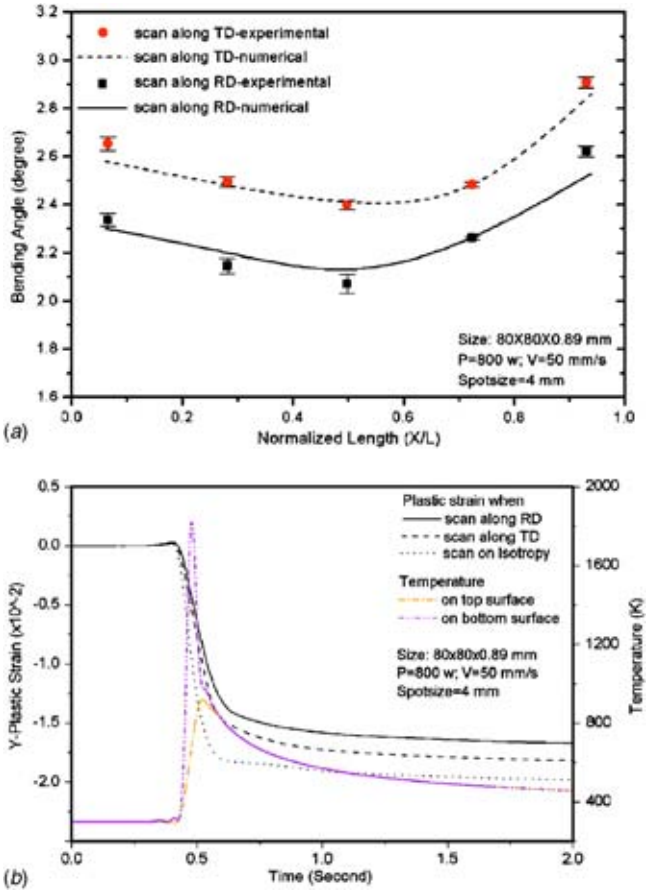

Fig. 8 (*a*) Numerical and experimental bending angles of 0.89 mm thick steel sheet with scanning along the RD and TD, respectively; and (*b*) simulated time history of the temperature on top and bottom surface, and the plastic strain in the *y* direction, which is perpendicular to the scanning path (results on isotropic sheets also included)

Besides the explanation stated above, another possible reason for the increasing relative bending angle difference between scanning along the RD and TD with speed is the effect of temperature change with speed on microstructure change. Figures 12(*a*) and 12(*b*) show the comparison of microstructure change under different scanning speeds (50 mm/s and 90 mm/s), respectively. It is shown that under both conditions the grains in the heat affected zone (HAZ) are refined due to the recrystalization. But the difference of grain refinement can be observed between different conditions. When the scanning speed is lower, the higher energy input makes the temperature and plastic strain larger so that the grain refinements are much better than the case of higher speed. As a result, the anisotropy effect relative to the bending angle will increase with the scanning speed.

4.5 Anisotropic Effect Under Different Laser Powers. Experiments under condition of constant scanning speed and various laser powers have been investigated when scanning is carried out either along the RD or TD. Since the scanning speed was kept constant, the effect of strain rate can be neglected. When laser power is higher, input heat energy and thus temperature rise is higher. As a result, flow stress decreased and bending angle increased with laser power increasing [Fig. 13(*a*)]. Since the temperature and flow stress effect on the bending deformation is almost the same for scanning along the RD or TD, the absolute difference of bending angle does not change much with power [Fig. 13(*b*)]. But again if the relative difference is calculated, it decreases from about 15% to 8% with power increase. This can be similarly explained as for the speed case. Higher temperature caused by the higher laser power allows the anisotropic material to more actively recrystallize while being formed, and thus ne-

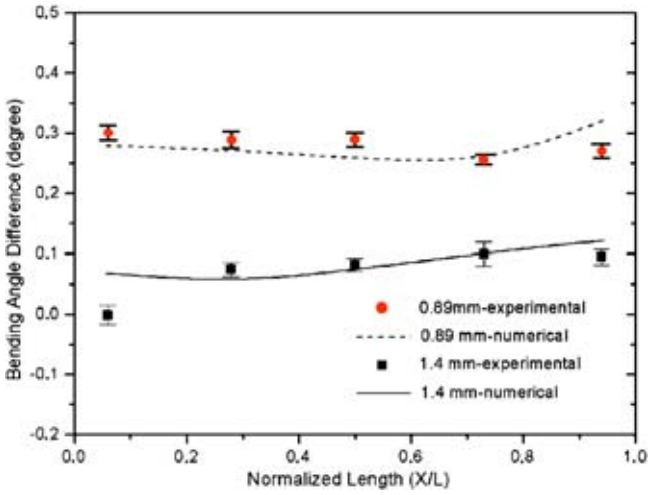

Fig. 9 Numerical and experimental bending angle difference between scanning along the RD and TD (for 80×80×1.4 mm, *P*=1200 W, *V*=50 mm/s, spot size=6 mm; and for 80×80×0.89 mm, *P*=800 W, *V*=50 mm/s, spot size=4 mm)

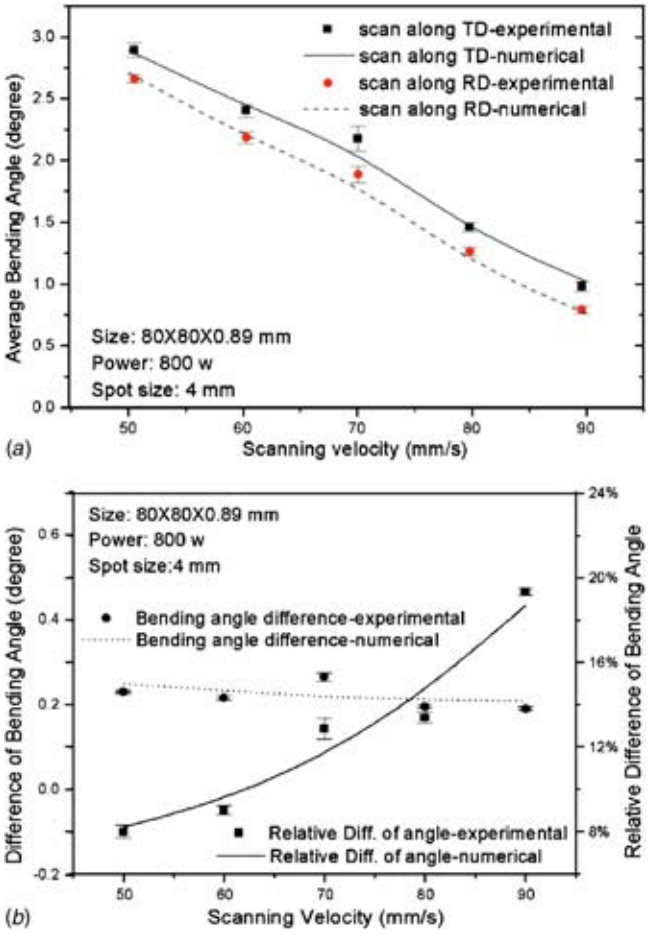

Fig. 10 (*a*) Bending angle and (*b*) differences of bending angle between scans along the RD and TD (constant laser power and varying speed)

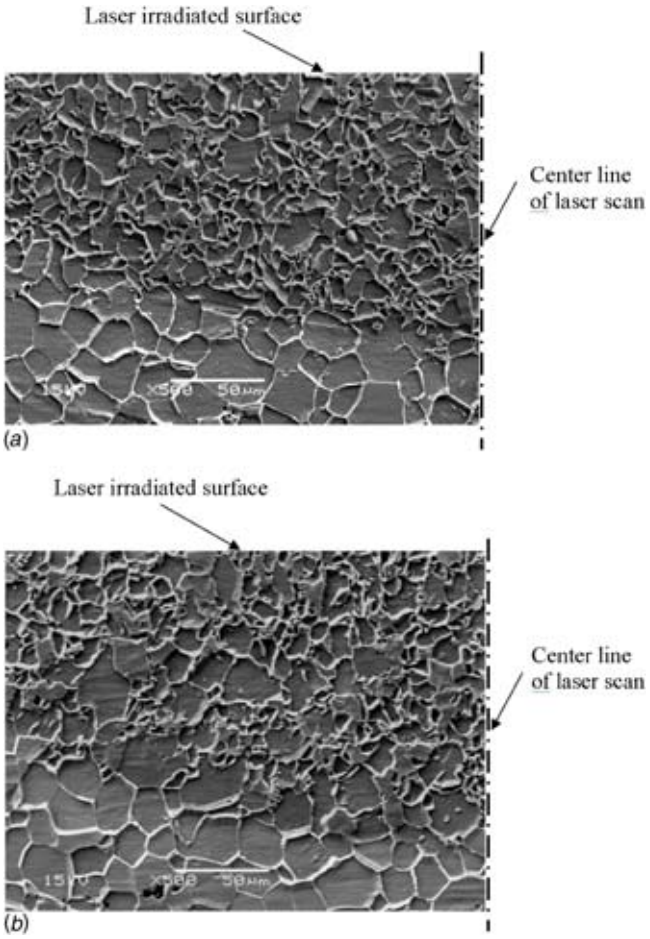

Fig. 12 SEM micrographs of the cross section perpendicular to the scanning path, showing the heat affect zone (HAZ) (dark colored, no melting involved) and the grain refinement in the HAZ under the conditions of (*a*) *P*=800 W, *V*=50 mm/s, and (*b*) *P*=800 W, *V*=90 mm/s

gates part of the anisotropy effect. So when the laser power increases while keeping a constant scanning speed, the relative difference of bending angle between scanning along the RD and TD will decrease. The trend shown in Fig. 13(*b*) is consistent based on both experimental and numerical results.

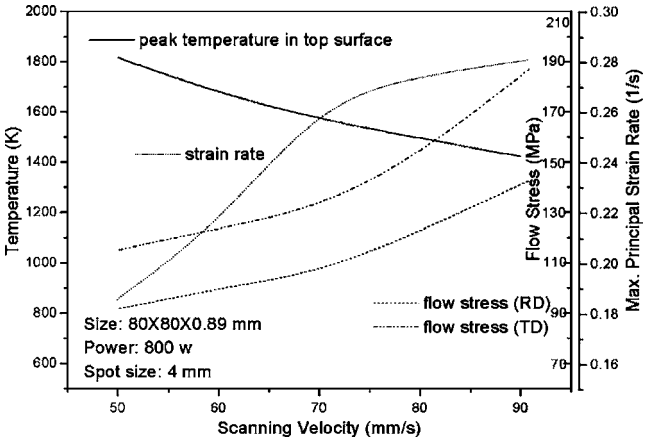

Fig. 11 Simulated peak temperature strain rate, and yield stress when scanning along the rolling direction and transverse direction

4.6 Anisotropic Effect in Multiscan Laser Forming. For laser forming to become a practical production or rapid prototyping tool, multiscan, that is, scanning the workpiece repeatedly by the laser, is necessary in order to achieve the required magnitude of deformation. Figure 14(*a*) shows the comparison of experimentally measured bending angles with simulation results for a 10-scan laser forming process under a condition of $P=800$ W and $V=50$ mm/s. Sufficient time was waited between scans to go back to room temperature and a graphite coating was applied to the scanning surface between scans to approach uniform laser power absorption. It is seen that the bending angle increases with multiscans either along the RD or TD. Figure 14(*b*) shows the difference and the increment of difference of bending angles when scanning along the RD or TD under multiscans. The difference of bending angle increases with the number of scans because the difference resulting from each scan accumulates. But the increment of bending angle difference decreases and almost reaches zero when it is over 8 scans, which clearly shows that the anisotropic effect decreases with the number of scans increasing. This phenomenon can be explained in two aspects. First it is due to the effect of flow stress. It is known that with multiple scans, flow stress increases due to the increased plastic strains. When scanning along the TD, larger *y*-plastic strain (along the RD) makes the flow stress in the RD increase and the increment is larger than that of the TD when scanning along the RD. As a consequence,

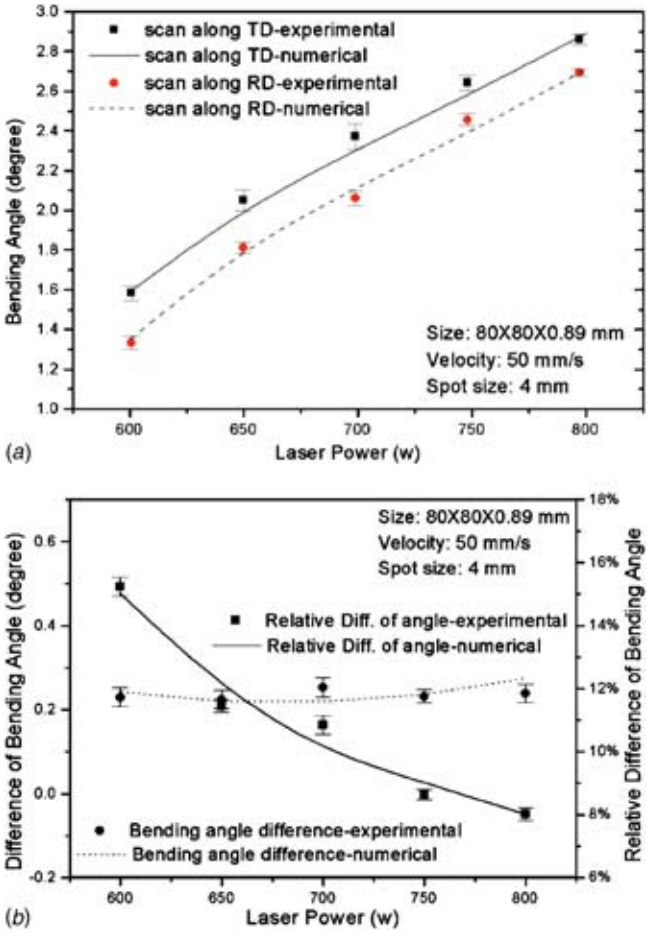

Fig. 13 (*a*) Bending angle and (*b*) differences of bending angle between scans along the RD and TD (constant speed and varying power)

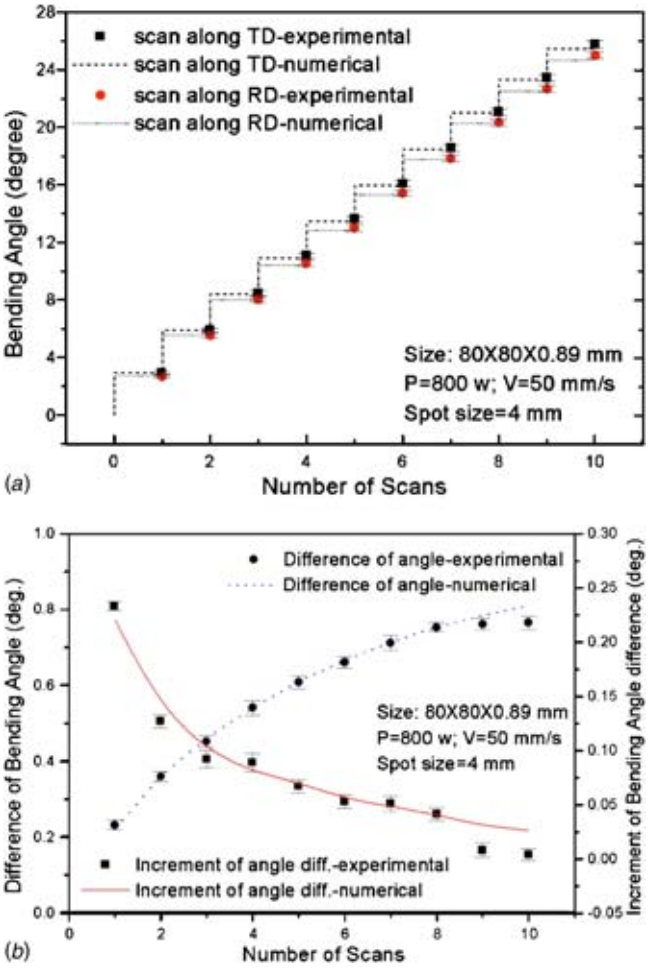

Fig. 14 (*a*) Bending angle and (*b*) differences and increment of difference of bending angle between scans along the RD and TD in multiscan laser forming

the difference of flow stress between the RD and TD decreases when the number of scans increases. Another reason is the recrystallization occurred repeatedly in the multiple scan process. By recrystallization, the deformed grain microstructure is gradually recovered and the anisotropy resulting from cold rolling decreases.

5 Conclusions

The plastic anisotropy of cold-rolled mild steel sheet with different rolling reductions used in laser forming was measured in terms of *R*-values via uniaxial tensile tests; and associated textures were characterized by EBSD. The results are in agreement with that based on the texture evolution theory. Effects of the plastic anisotropy on laser forming under different conditions were experimentally and numerically investigated, and the numerical results agree with the experimental ones. The anisotropic effect increases with the rolling reduction. If scanning velocity increases while the laser power is kept constant, the anisotropic effect increases relative to the bending deformation, primarily due to the lower temperature and smaller plastic strain for recrystallization. If the scanning velocity is kept constant while laser power increases, higher temperature will make the anisotropic effect smaller relative to the deformation. In the multiscan laser forming process, repeated recrystallization during multiple scanning and different increments of flow stress in the RD and TD reduce the anisotropic effect.

References

[1] Scully, K., 1987, "Laser Line Heating," J. Ship Prod., **3**(4), pp. 237–246.

[2] Vollertsen, F., 1994, "Mechanisms and Models for Laser Forming," *Laser Assisted Net Shape Engineering, Proceedings of the LANE'94*, B. Meisenbach, ed., **1**, pp. 345–360.

[3] Sprenger, A., Vollertsen, F., Steen, W. F., and Watkins, K., 1994, "Influence of Strain Hardening on Laser Bending," *Laser Assisted Net Shape Engineering, Proceedings of the LANE'94*, B. Meisenbach, ed., **1**, pp. 361–370.

[4] Li., W., and Yao, Y. L., 2000, "Numerical and Experimental Study of Strain Rate Effects in Laser Forming," ASME J. Manuf. Sci. Eng., **122**, pp. 445–451.

[5] Cheng, J., and Yao, Y. L., 2002, "Microstructure Integrated Modeling of Multiscan Laser Forming," ASME J. Manuf. Sci. Eng., **124**, pp. 379–388.

[6] Liao, K. C., Friedman, P. A., Pan, J., and Tang, S. C., 1998, "Texture Development and Plastic Anisotropy of B. C. C. Strain Hardening Sheet Metals," Int. J. Solids Struct., **35**(36), pp. 5205–5236.

[7] Hill, R., 1948, "A Theory of the Yielding and Plastic Flow of Anisotropic Metals," Proc. R. Soc. London, Ser. A, **193**, p. 281.

[8] Gotoh, M., 1977, "A Theory of Plastic Anisotropy Based on a Yield Function of Fourth Order (Plane Stress State)-I and II," Int. J. Mech. Sci., **19**, pp. 505–520.

[9] Barlat, F., and Lian, J., 1989, "Plastic Behavior and Stretch Ability of Sheet Metals Part I: A Yield Function for Orthotropic Sheet under Plane Stress Conditions," Int. J. Plast., **5**, p. 51.

[10] Hill, R., 1990, "Constitutive Modeling of Orthotropic Plasticity in Sheet Metals," J. Mech. Phys. Solids, **38**, pp. 405–417.

[11] Hosford, W. F., 1996, "On the Crystallographic Basis of Yield Criteria," Textures Microstruct., **26–27**, pp. 479–493.

[12] Taylor, G. I., 1938, "Plastic Strain in Metals," J. Inst. Met., **62**, pp. 307–324.

[13] Kocks, U. F., and Chandra, H., 1982, "Slip Geometry in Partially Constrained Deformation," Acta Metall., **30**, pp. 695–709.
[14] Gilormini, P., 1989, "The Theory of Rate Sensitive Pencil Glide Application to Rolling Textures," Acta Metall., **37**(7), pp. 2093–2101.
[15] Kocks, W. K., Tome, C. N., and Wenk, H. R., 1998, *Texture and Anisotropy-Preferred Orientations in Polystals and Their Effects on Material Properties*, Cambridge University Press, London, pp. 48–112.
[16] Raabe, D., and Lucke, K., 1994, "Rolling and Annealing Textures of BCC Metals," Mater. Sci. Forum, **157–162**, pp. 597–610.
[17] Raabe, D., 1995, "Simulation of Rolling Textures of b.c.c. Metals Considering Grain Interactions and Crystallographic Slip on {110}, {112}, and {123} Planes," Mater. Sci. Eng., A, **197**, pp. 31–37.
[18] ASTM, 2002, "Metals Test Methods and Analytical Procedures," *Annual Book of ASTM Standards, 03.01*, ASTM International, Philadelphia, PA.
[19] Daniel, D., and Jonas, J. J., 1990, "Measurement and Prediction of Plastic Anisotropy in Deep-Drawing Steels," Metall. Trans. A, **21A**, pp. 331–343.
[20] Bao, J., and Yao, Y. L., 2001, "Analysis and Prediction of Edge Effects in Laser Bending," ASME J. Manuf. Sci. Eng., **123**, pp. 53–61.